SYNTHESIS, CHARACTERIZATION, AND APPLICATION OF Fe_3O_4 NANOPARTICLES AS A SIGNAL AMPLIFIER ELEMENT IN SURFACE PLASMON RESONANCE BIOSENSING

I Putu Tedy Indrayana[1*], **Margaretha Tabita Tuny**[2], **Rachmad Almi Putra**[3], **Juharni**[4], **Edi Suharyadi**[4], **Takeshi Kato**[5], **Satoshi Iwata**[5]
[1] *Physics Study Program, Faculty of Natural Science and Engineering Technology, Universitas Halmahera – INDONESIA*
[2] *Forestry Study Program, Faculty of Natural Science and Engineering Technology, Universitas Halmahera - INDONESIA*
[3] *Physics Study Program, Faculty of Engineering, Universitas Samudra – INDONESIA*
[4] *Department of Physics, Faculty of Mathematics and Natural Science, Universitas Gadjah Mada – INDONESIA*
[5] *Institute of Materials and Systems for Sustainability, Nagoya University - JAPAN*
[*] e-mail: tedyindrayana@gmail.com

ABSTRACT

The Fe_3O_4 nanoparticle has potential applications to be active materials for biosensor. This research was aimed at synthesizing, characterizing, and applying Fe_3O_4 nanoparticles for signal amplification element in Surface Plasmon Resonance (SPR) biosensing. The synthesis was carried out by using the coprecipitation method at a temperature of 80°C for 60 minutes. NaOH of 5 molars was used as a precipitating agent. The Fe_3O_4 nanoparticles were characterized for their microstructure by using X-Ray Diffraction (XRD) and Transmission Electron Microscopy (TEM) techniques. The crystallinity of nanoparticles is 87% and the crystallite size is 15.70 nm. The shape of Fe_3O_4 is nearly spherical. The optical properties were characterized by using Fourier Transform Infrared Spectroscopy (FTIR) and Specular Reflection UV-Vis Spectroscopy (SR UV-Vis). There were vibrations of Fe^{3+}-O and Fe^{2+}-O bonds at characteristic frequencies of 586.86 cm^{-1} and 422.64 cm^{-1}. The direct and indirect optical gap energies were 3.43 eV and 3.10 eV. The magnetic properties measured by Vibrating Sample Magnetometer (VSM) confirmed that Fe_3O_4 was ferrimagnetic. The Fe_3O_4 was successful to be applied as a signal amplifier for SPR-based biosensors due to their optical and magnetic properties. The SPR angle shifted to a higher value and the change was 3.57°.

Keywords: *Fe_3O_4; Iron Sand; Signal Amplifier; SPR Biosensing*

INTRODUCTION

In recent years, the development of biosensor technology has been done rapidly for multiple purposes due to its potential applications in many fields, such as environmental monitoring, healthcare, chemical and biological analysis, and food safety control. For those applications, there are many kinds of a biosensor which have been developed, such as chemical, electrochemical, electro-impedance, magnetic, piezoelectric, optical, and thermal biosensor (Mehrotra, 2016). Due to rapid progress in the synthesis, fabrication, and characterization of the nanomaterials allow the development of nanomaterial integrated biosensor technology nowadays. For instance, Surface Plasmon Resonance (SPR) based biosensor utilizing Graphene-MoS_2 for detection urea (Jamil, et al., 2017); electrochemical biosensor based on gold nanoparticle for detection of polynucleotide kinase assay (Cui, et al., 2018); and nano-hybrid integrated in electrochemical biosensor for glucose detection (Batool, et al., 2019).

Among a different kind of biosensor, optical biosensor based nanomaterials have been attracted much interest of the researchers due to its advantages, such as high affinity, high selectivity, ease of use, allows to use for detection of multiple analytes in the same time, and allows for conducting a real-time measurement (Antiochia, et al., 2016). One of the most famous optical biosensor based nanomaterials is an SPR based biosensor due to its tremendous applications and ease of use for monitoring bio-specific interaction directly without using labeled molecules (Salazar, et al., 2018). SPR-based biosensor principally works by the resonance between the evanescent wave and the surface plasmon wave while absorbing a fraction of the incident light comes from the light source, i.e. laser. This phenomenon occurs at a specific critical incident angle θ_{sp} and a wavelength of light λ. The value of θ_{sp} strongly depends on the refractive index of the sensing dielectric medium (Ekariyani, et al., 2016; Oktivina, et al., 2017; Widayanti, et al., 2018). In this case, the sensing dielectric medium involves the nanomaterials used in the SPR system.

Many types of nanomaterials have been used for that purpose. The three oxide nanomaterials, i.e., TiO_2, SiO_2, and SnO_2 have been used to be a cover for the SPR active metallic layer to increase the sensitivity of the sensor (Singh, et al., 2013). Experimentally, (Ekariyani, et al., 2016; Oktivina, et al., 2017) had used Fe_3O_4 nanoparticles as an active material for increasing the biosensor response. In 2018 (Widayanti, et al., 2018) had conducted a computational study on the use of the core-shell structure of Fe_3O_4-Au as an active material for enhancing the sensitivity of the sensor.

Since a century, the Fe_3O_4 is still being an attractive material due to its super-astonishing physicochemical properties which enable the Fe_3O_4 to be applied in many fields of technologies. The properties include surface charge density, surface area, porosity, functional groups, and crystallite size (Tareq, et al., 2019). For this reason, here we present an experimental study about the application of the Fe_3O_4 nanoparticles as an element for signal amplification of SPR-biosensing. We have been done some optimization of the synthesis and characterization of the Fe_3O_4 nanoparticles from local iron sand in our research group. In this paper, we provide a detail explanation about the relation between physical properties (except magnetic properties) of the Fe_3O_4 nanoparticles and its role in the biosensing process.

METHODS AND MATERIALS

Raw Materials Synthesis

The source of Fe used in this research is local iron sand which was taken from Wari Ino Beach, Halmahera Utara. The iron sand was prepared through a purification process for removing impurities. HCl (Mark Sigma-Aldrich) solution of 37% (12M) was used to dissolve the iron sand for the formation of $FeCl_2$ and $FeCl_3$ solutions. The coprecipitate was NaOH (Merck Emsure) purchased from LPPT UGM, Yogyakarta. The coprecipitate was used for the formation of metal hydroxide compounds, such as $Fe(OH)_3$ and $Fe(OH)_2$ in the coprecipitation process.

Synthesis of the Fe_3O_4 Nanoparticles

Synthesis of the Fe_3O_4 nanoparticles was started by preparing Fe solution. For this purpose, 25 grams of purified iron sand was dissolved by using 30 ml HCl (12M). The mixture was stirred constantly while heated up to 70°C. The temperature of the mixture was kept constant for about 30 minutes. The yellowish dark solution was obtained after the stirring process. This solution was filtered by using Whatman paper.

The synthesis of the Fe_3O_4 nanoparticles was carried out by using the coprecipitation method at a temperature of 80°C for 60 minutes. The concentration of NaOH solution was 5M within 75 ml distilled water. First of all, the NaOH solution was heated up to 80°C. At this temperature, the Fe solution of 20 ml was dropped wisely using a glass pipette to the NaOH solution while stirring at a constant rate of 500 rpm. In this stage, the constant dropping technique is important because the rate of dropping Fe solution will determine the rate of nucleation of the Fe_3O_4 and influence the size, further their distribution. During synthesis, a black solution will be obtained. This would be the first indicator of the success of the synthesis. After 60 minutes, the temperature of the solution was dropped down naturally until it reaches room temperature. During this stage, the solution was placed on the magnetic table (Merk Kanetsu) of 10 kOe to trigger a separation between the slurry of the Fe_3O_4 and the solvent. If the synthesis was a success, so the slurry will be separated quickly with its solvent. A clear solvent will be provided and black slurry will precipitate at the bottom of the glass. The slurry was rinsed by using distilled water of 200 ml in volume 5 times to ensure that the impurities had removed.

The black slurry can be tested by using an external magnetic bar. If the slurry is a magnetic than the slurry will be attracted by the magnetic field induced by a bar magnet. The slurry within the petri disk was heated up in an oven at a constant temperature of 100°C for 4 hours. After heating, black chips of nanoparticles will be obtained and they have to be crushed by using mortar and pestle to obtain black powder Fe_3O_4. The powder might also be reddish-brown which indicates that the sample not totally in the Fe_3O_4 phase. It might be composed of some oxidation phases of Fe_3O_4.

Sample Characterizations

The sample of Fe_3O_4 was characterized by its crystal structure and microstructural parameters by using X-Ray Diffraction Technique (XRD) (Diffractometer Merk PANanalytical-Expert Pro) with scan range 2θ of $20^\circ - 80^\circ$, scan step of 0.002°, and in reflection mode using Cu-Kα1 radiation. Grain morphology and the electron diffraction pattern of the sample were characterized by using Transmission Electron Microscopy (TEM) (Merk JEOL JEM-1400) coupled with Electron Diffraction

Microscopy with a voltage of 120V. The vibration spectra of the functional groups were recorded by using Fourier Transform Infrared Spectroscopy (FTIR) (Merk Paragon 1000PC Perkin Elmer) with a wavenumber range of 450 cm^{-1} – 4000 cm^{-1}. The absorbance spectra of the sample were recorded by using UV-Vis Spectroscopy (Merk Pharmaspec UV-1700) with a wavelength of 200 nm – 800 nm. The magnetic hysteresis curve was recorded by using Vibrating Sample Magnetometer (Merk Riken Denshi Co Ltd.). The external magnetic field used for this measurement was in the range of (-15) kOe – (+15) kOe. The measurement was conducted at room temperature.

Preparation and SPR Measurement

Preparation, in this case, was conducted for preparing gold thin film which deposited on the surface of the prism. For this purpose, this research used BK7 type prism in the form of a hemicylindrical prism.

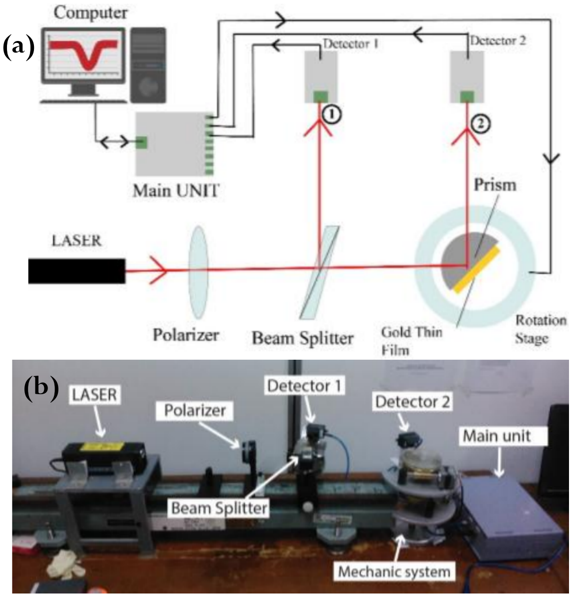

Figure 1. Instrumentation set-up of SPR-based biosensor: (a) block diagram of the instrument and (b) real set-up of the instrument (Laksono, et al., 2018)

First of all, the TIR (Total Internal Reflection) curve of the prism (Prism/Air system) was recorded by using SPR based biosensor instrument (see Fig.1 for instrumentation set-up). The instrument consisted of He-Ne laser (OSK Ogawa Seiki Co Ltd) of a wavelength of 632.8 nm and power of 3 mW, a polarizer, a beam splitter, and two light detectors. According to the TIR curve (reflectivity v.s incident angle of light), the critical angle of the prism (θc) can be measured and then its refractive index n_p can be calculated by using Equation (1):

$$n_p = \frac{1}{\sin\theta_c} \,. \tag{1}$$

Secondly, deposition of 15 mg gold (Merk Fine Gold-Au Antam 999.9) on the plat surface of the hemicylindrical prism was carried out by using a thermal evaporation method. A thin layered gold, in this case, has a role to be a conductive layer for sensing. Thirdly, the ATR (Attenuated Total Reflection) curve for this system (Prism/Au/Air) was recorded with incident angles in a range of $30.00^o – 60.00^o$ (accuracy of $\theta = \pm 0.01^o$).

Thirdly, the preparation of the Fe_3O_4 solution was carried out by dissolving 60 mg Fe_3O_4 powder in 5 ml ethanol. The solution was homogenized in an ultrasonic chamber for about 14 minutes to make sure that the Fe_3O_4 powder dissolved by the ethanol. This solution was then deposited on the gold layer by using a spray method for about 3 times. The last, the ATR curve of this system (Prism/Au/Fe_3O_4/Air) was recorded with incident angles in a range of $30.00^o – 60.00^o$.

RESULTS AND DISCUSSIONS

Microstructural Properties

The crystal structure and microstructural parameters of the Fe_3O_4 nanoparticles were justified from the XRD pattern obtained from the characterization (see Fig. 2). The XRD pattern of sample shows six diffraction peaks at the diffraction angles 2θ of 30.21^o; 35.47^o; 43.13^o; 53.45^o; 57.03^o; and 62.63^o which refer to the diffraction peaks of (220); (311); (400); (422); (511); and (440), consecutively. Those are the characteristic diffraction peaks belong to the Fe_3O_4 phase based on the standard diffraction data JCPDS (Joint Committee for Powder Diffraction Set) card no 11.0614. The diffraction pattern of Fe_3O_4 is also in agreement with the result reported by (Malega, et al., 2018) which indicates that the sample was a polycrystalline material in nature. The crystallinity of the sample was up to 87.33%.

The diffraction peaks were high and sharp indicate that the sample much crystalline in nature. Noises occurring in the diffraction pattern were mainly affected by the filter material within the instrument. It also described the diffraction pattern of nano-sized particles. Moreover, the highest intensity of the diffraction peak belongs to a peak of (311) which indicates that the largest preferential growth direction of the crystallite to [311]. Quantitatively, a comparison of the preferential growth direction of the crystallite Fe_3O_4 can be justified based on the texture coefficient (*TC*) value which is displayed in the index. The *TC* was calculated by using equation provided by (Hafez, et al., 2014). In short, the lack of crystallite orients to the direction of [220]; [400]; [511]; [440]; and further [422].

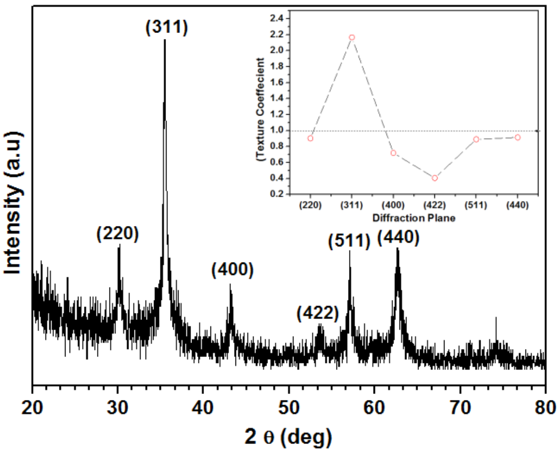

Figure 2. XRD pattern of Fe_3O_4 nanoparticles. (Index: plot of texture coefficient for each diffraction peak)

Single phase Fe_3O_4 nanoparticles with cubic crystal structure have been obtained in the sample with no other impurities. The sample crystallize is in the space group of $Fd\bar{3}m$. Due to the occupancy of the octahedral and tetrahedral sublattice by Fe^{2+} and Fe^{3+} cations so the Fe_3O_4 nanoparticle has an inverse spinel structure within the cubic closed-pack structure. This is supported by the appearance of the diffraction peaks of (220), (400), and (422). Those reflection planes are known very sensitive to cation distribution of ferrite within their spinel structure (Heiba, et al., 2016). The peak of (220) depends on cations occupying the tetrahedral sublattice, while peaks of (400) and (422) depend on cations occupying the octahedral sublattice (Huili, et al., 2014).

The values of microstructural parameters of the Fe_3O_4 nanoparticles are tabulated completely in Table 1. Regarding the crystal structure, the lattice parameter of the Fe_3O_4 was obtained 8.3805 Å. This value is shorter than that provided in JCPDS No 11-0614, but it is longer than the lattice parameter reported by (Malega, et al., 2018). In the case of the crystal structure, a line broadening occurred on the diffraction peak indicates the existence of microstrain in the unit cell along the direction of [311]. The value was calculated to be $2.183 \cdot 10^3$/lines and might be affected by factors, i.e., no perfect nucleation of the crystal seed and cation distribution due to cationic position within the unit cell of the crystal.

The imperfect crystal structure owned by Fe_3O_4 nanoparticles was also indicated by dislocation density. Its value was $4.056 \cdot 10^{-3}$ nm^{-2} along the direction of [311]. Moreover, the crystal density of the Fe_3O_4 nanoparticles was 5.235 $gram/cm^3$ in agreement to the result reported by (Malega, et al., 2018).

The crystallite size of nanoparticles was calculated by using Scherer's equation provided in (Mote, et al., 2013). The crystallite size of the Fe_3O_4 nanoparticle was 15.70 nm in agreement with the result reported by (Salviano, et al., 2018) and smaller than that reported by (Malega, et al., 2018). A small crystallite size allows the Fe_3O_4 having unique physicochemical properties, such as soft magnetic, higher bandgap energy, and larger specific surface area. By using Equation (2), the specific surface area of the Fe_3O_4 was calculated to be $73.00 \cdot 10^4$ $cm^2/gram$,

$$S_A = \frac{6}{\rho \cdot t} \quad . \tag{2}$$

where S_A is the specific surface area ($cm^2/gram$), ρ refers to the crystal density of the Fe_3O_4 ($gram/cm^2$), and t is the crystallite size (cm) (Dhas, et al., 2015). A larger specific area of the nanoparticle is due to a smaller crystallite size. Larger specific surface area is very advantageous for the chemical reaction on the surface of the nanoparticles. The rate of the chemical reaction can be tuned by increasing the surface area of the nanoparticles.

Table 1. Microstructural parameters of Fe_3O_4.

No.	Microstructural Parameters	Value
1.	Crystallinity (%)	87.33
2.	Lattice parameter a (Å)	8.3805
3.	Microstrain ε (311) plane ($\cdot\ 10^{-3}$)	2.183
4.	Dislocation density δ (311) plane ($\cdot\ 10^{-3}$ nm^{-2})	4.056
5.	X-Ray density ρ_x ($gram/cm^3$)	5.235
6.	Crystallite size t (nm)	15.70
7.	Specific surface area S_a ($\cdot\ 10^4$ $cm^2/gram$)	73.00

Morphology and Electron Diffraction

The profile morphology of the nanoparticles was recorded by using TEM and the micrograph can be displayed such as Fig.3a. The micrograph tells that the formation of agglomerated nanoparticles with variation in the grain size due to no perfect nucleation occurred during the synthesis. The grain size of the nanoparticles was in the range of 10 – 40 nm due to their broad distribution. This result is in agreement with the crystallite size obtained from XRD analysis. The grains were spherical-like in shape.

Correspondingly, agglomeration experienced by the nanoparticles is affected by an absence of surfactant which disperses the grain of nanoparticles. Naturally, a sample of Fe_3O_4 is a magnetic material in nature so that strong magnetic interaction between grains drives the agglomeration. In the presence of surfactant, the magnetic interaction between grains might be decreased due to decreasing surface tension of the nanoparticles caused by the nonmagnetic property of the surfactant. In the case of its application for biosensor, the nanoparticles have to be polydisperse indeed monodispersing. Some technical efforts have been done by researchers for improving the dispersibility of the nanoparticles, such as encapsulation of Fe_3O_4 by using polymer (Wang, et al., 2010); sparking the iron salts solution during synthesis by using N_2 gas (Ramadan, et al., 2011; Tajabadi & Khosroshahi, 2012); addition of ultrasonic radiation during synthesis of the Fe_3O_4 nanoparticles (Rahmawati , et al., 2018); and addition heat treatment, i.e., calcination, annealing, further sintering after the synthesis.

The electron diffraction profile owed by the Fe_3O_4 nanoparticles can be displayed by Fig.3b. This selected area of the electron diffraction (SAED) image shows that the appearance discrete diffraction rings, exactly in the form of spotted-ring with different intensity. This pattern indicated that a sample of the Fe_3O_4 nanoparticles is polycrystalline material in nature. The rings can be identified as the diffraction by electron on the reflection planes of (220); (311); (400); (422); (511); and (440). The intensity of electron diffraction by reflection plane (311) is the largest which indicates that the density of electron along this direction is the largest. This evidence coincides with the result of the XRD analysis.

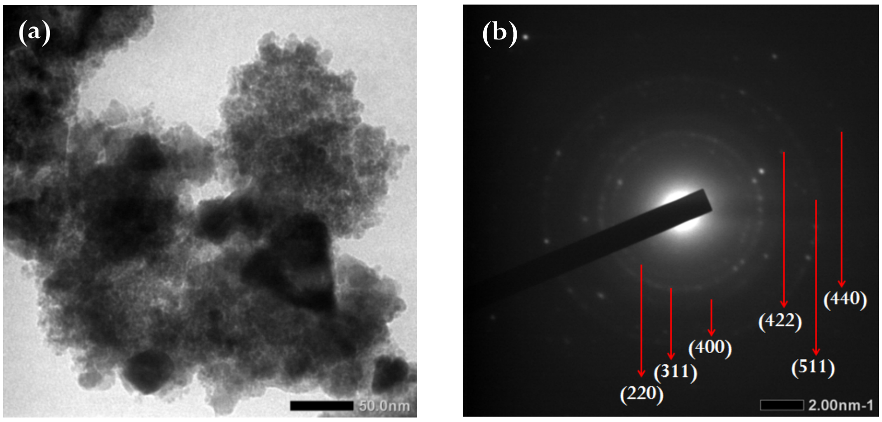

Figure 3. (a) TEM micrograph and (b) electron diffraction profile (SAED image) of Fe_3O_4.

Functional Groups Vibration Spectra

The functional group's vibration spectra of the Fe_3O_4 nanoparticles can be displayed by Fig.4. According to the spectra, two intense absorption peaks were investigated in a wavenumber range of 400 cm^{-1} – 700 cm^{-1}. Those are the stretching vibrations by Fe^{2+}-O bond (422.64 cm^{-1}) and Fe^{3+}-O bond (586.86 cm^{-1}) in the octahedral and tetrahedral sublattice, consecutively. This fact supported that a successful formation of the Fe_3O_4 phase occurs in this synthesis.

The absorption peaks in the region of 1300 cm^{-1} – 1650 cm^{-1} were associated with the vibration O-H bending (1370 cm^{-1} and 1633.78 cm^{-1}). Hence, the most intense absorption occurs in the region of 2900 cm^{-1} – 3800 cm^{-1} was assigned as O-H stretching vibration (3437.06 cm^{-1}). The existence of those functional groups indicated that the Fe_3O_4 nanoparticles still bind with water molecules on their surface. Naturally, the Fe_3O_4 nanoparticles are hygroscopic; therefore they are easy to interact with a water molecule and the oxidation as its consequence. A weak absorption peak at a wavenumber of 2371.20 cm^{-1} was assigned as an asymmetric stretching vibration of the C-H bond due to binding between the Fe_3O_4 nanoparticles and CO_2 free molecules in the atmosphere.

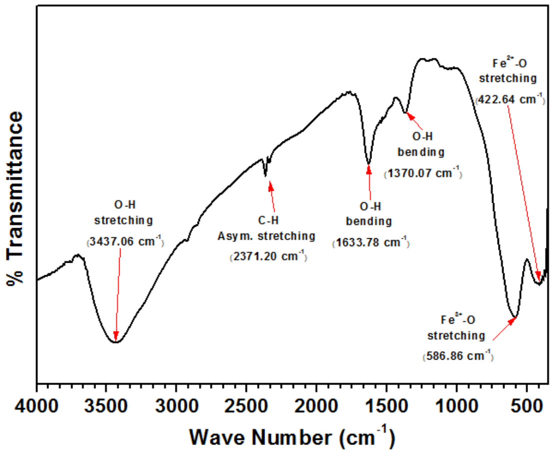

Figure 4. The FTIR spectra of Fe_3O_4 nanoparticles.

Magnetic Properties

The magnetic hysteresis curve (see Fig.5) of the Fe_3O_4 was recorded at room temperature (≈ 300K). By applying an external magnetic field of 14.677 kOe, so the maximum specific magnetization was 27.73 emu/gram and the specific remanence magnetization was 5.29 emu/gram. Accordingly, the sample of nanoparticles was soft-ferrimagnetic in nature with a small coercivity of 94.29 Oe. Due to broad size distribution, the nanoparticle has no superparamagnetic properties. Some papers have been reported that the Fe_3O_4 can perform superparamagnetic property at room temperature (Ramadan, et al., 2011; Chaki, et al., 2015; Salviano, et al., 2018). Mainly, the magnetic properties of the nanoparticles are affected by many factors, i.e., crystal structure, cation distribution of the nanoparticles, impurities, and crystallite size with their distribution. Due to a quantum confinement effect at the nano-scale, therefore, the magnetic properties performed by the Fe_3O_4 nanoparticles strongly correlated to their crystallite size.

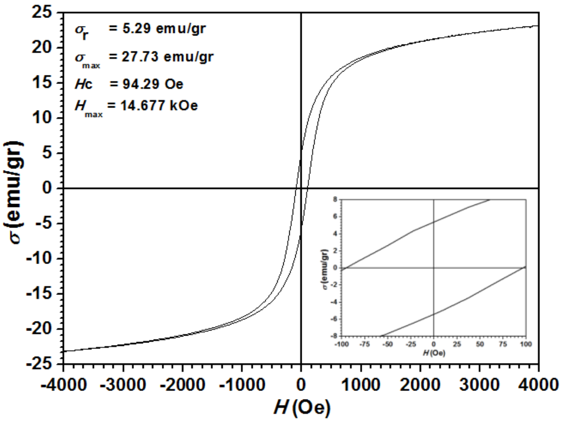

Figure 5. The hysteresis curve of Fe_3O_4.

Optical Properties

The optical properties of the Fe_3O_4 can be studied according to the absorbance and reflectance spectra versus photon wavelength. That spectrum can be displayed in Fig.6. There was a maximum absorbance peak at a wavelength of 332.76 nm that attributed by the maximum absorption of photon energy by electron while exciting from the highest state of the conduction band to the lowest state of the valence band. A broad absorption peak justifies that interaction phenomena occurred between photons and the nanoparticles with different in size.

Accordingly, the specular reflectance of the Fe_3O_4 occurred in a wavelength region of 200 nm – 800 nm was not uniform even zero. This was caused by a sample of the Fe_3O_4 optically not transparent due to the morphological structure of the Fe_3O_4. The reflectance values ware varies with photon wavelength. In a shorter wavelength, there is a small plateau and then it drops down until finding a peak at a wavelength of 315.22 nm. Another small plateau was also observed at a longer wavelength region (λ_{photon} > 750 nm). The reflectance feature of the Fe_3O_4 is the characteristic of polycrystalline material due to no uniform radiant power of photon in the reflection plane. In short, the collected incident photons might be restricted by the reflection direction of the crystal planes.

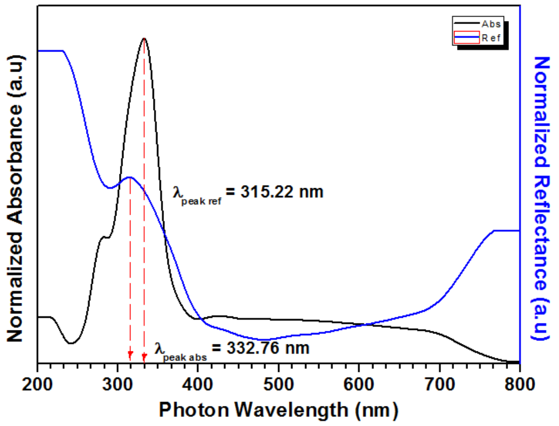

Figure 6. Absorbance and reflectance spectra of Fe_3O_4 as a function of photon wavelength.

Quantitatively, the optical properties of the Fe_3O_4 nanoparticles can also be studied regarding the values of optical gap energy. In this case, by considering the excitation process of an electron from the conduction band to the valence band, so we analyzed the optical band gap energy into two types, i.e., direct and indirect optical gap energies. Direct optical gap energy is measured when electron excited from the highest state of the conduction band to the lowest state of the valence band in a corresponding *k* (crystal momentum) value. On the other hand, the indirect optical gap energy is measured when electron excited from the highest state of the conduction band to the lowest state of valence band with different *k* values. Therefore, during this excitation electron get an interaction with phonon for jumping into a targeted position in the valence band. Both direct and indirect optical gap energies of the Fe_3O_4 nanoparticles were calculated by using Tauch's method as explained in detail in (Ghandoor, et al., 2012; Abd, et al., 2016; Indrayana, et al., 2019). Tauch's plot is displayed in Fig. 7.

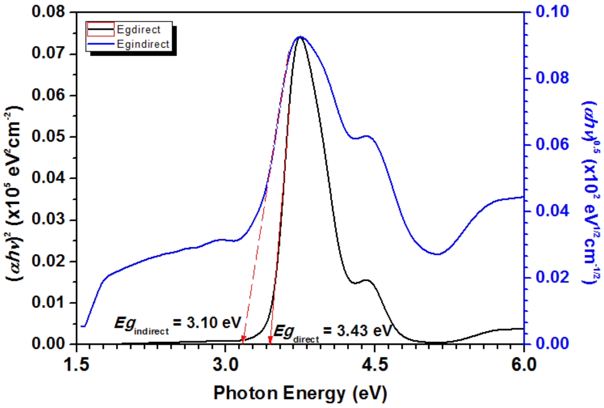

Figure 7. Tauch's plot of Fe_3O_4 for determining direct and indirect optical gap energy.

The direct optical gap energy is larger than the indirect optical gap energy due to nanoparticles in nature. Another reason came from the nature of mathematical relation of the Tauch' equation at which order n = 2 fits for lower photon energy and n = 1/2 fits for higher photon energy. The optical gap energies obtained in this research were larger than that reported by (Ghandoor, et al., 2012; Abd, et al., 2016) due to a different in crystallite size. Larger crystallite size provides smaller optical gap energy. Accordingly, the Fe_3O_4 nanoparticles can be classified into p-type semiconductor materials in case their optical gap energy smaller than 3 eV. The semiconductor material is a material where their bandgap containing Fermy level narrower than 3 eV. Hence, increasing the optical band gap will allow the material change to be an insulator.

The dielectric material is typically an insulator with a bandgap value bigger than 3 eV (Bain & Chand, 2017). Increasing the optical gap energy of the nanoparticles tends to decrease their dielectric loss (loss tangent – tanδ) due to a lowering of electron's tunneling probability to the conduction band from the valence band (Sati, et al., 2019). Hence, larger optical gap energy provides the stronger dielectric property of the Fe_3O_4. Therefore, the Fe_3O_4 nanoparticles are very suitable to be applied as active material in SPR-based biosensors. In case, the active material in SPR-based biosensor has to be a dielectric in nature.

The tail of the absorption edge in the electronic structure of the Fe_3O_4 might be experienced by the electronic structure of the Fe_3O_4 due to microstrain and defect occurring within the structure. As earlier discussion that microstrain can be induced by temperature, pressure, cation displacement, further impurities within the sample. Hence, the wideband tail of the absorption edge at the localized state can be assigned as Urbach energy. The Urbach energy refers to an electronic disorder near the band edge. The disorder due to a random distribution of defect in the crystal structure of the nanoparticles and onsite potential fluctuation (Sati, et al., 2019).

The Urbach energy can be calculated by extrapolation of the linear portion of the curve between natural logarithmic of absorption coefficient α and photon energy $h\upsilon$ as explained in detail by (Ghandoor, et al., 2012). The curve can be displayed in Fig.8. The Urbach energy of the Fe_3O_4 nanoparticle was 0.22 eV. This value smaller compared to the energy reported by (Ghandoor, et al., 2012). Principally, this energy is strongly affected by the crystallite size of the Fe_3O_4 nanoparticles due to a quantum confinement effect at the nano-scale structure.

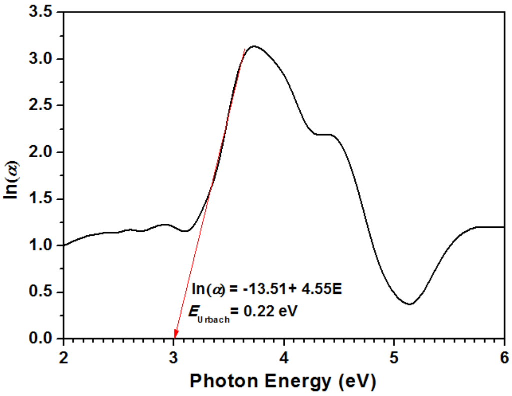

Figure 8. Urbach energy of Fe_3O_4 nanoparticles.

Application on SPR Based Biosensor

The application of the Fe_3O_4 nanoparticles for SPR-based biosensor was performed out by applying a conventional prism-based Kretschmann configuration. First of all, the BK7 hemicylindrical prims were recorded for its TIR curve to determine the critical angle θc and its refractive index np. The TIR curve of the prism is displayed by Fig.9. The critical incident angle of the prism was 43.85° and the calculated refractive index was 1.44.

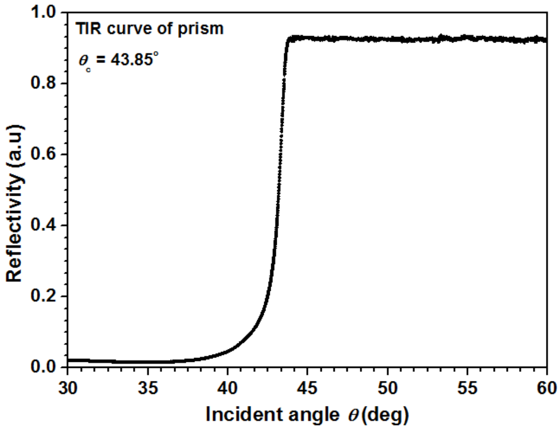

Figure 9. Total internal reflection curve of prism.

The Kretschmann configuration of this measurement used four layers system, such as prims/Au/Fe_3O_4/Air. Pictorially, it can be figured out by Fig. 10. The Au thin layer was deposited on the flat surface of the prism by using the evaporation method. The biosensor performance was performed by attenuated total reflection (ATR) curve as displayed in Fig.11.

According to Fig. 11, the reflectivity experiences attenuation in the region after the critical angle. First, the critical angle of the ATR curve after the addition of the Au layer was 44.24° and then it shifted to an angle of 44.71°. The reflectivity was attenuated. This phenomenon occurs when the intensity of the reflected light is attenuated and the conduction electrons of Au absorb incident photon energy. At this time, the surface plasmon resonance wave was generated at the interface between the Au surface and the dielectric medium. The dielectric medium, in this case, is the Fe_3O_4. The energy is transferred from photon to the conduction electrons in a metal. This affects the reducing intensity of the reflected light in the region of resonance wavelength.

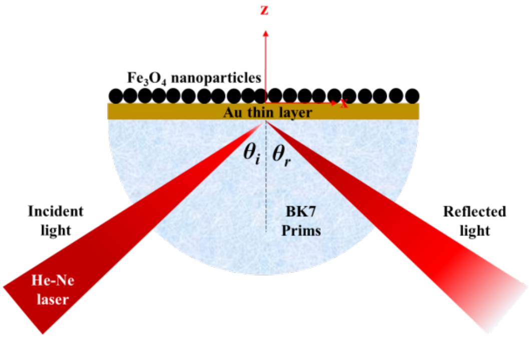

Figure 10. Kretchmann SPR configuration.

According to Fig. 11, dip at the lowest reflectance intensity of the ATR curve was shifted to a larger incident angle by 3.57°. The intensity also changed to a smaller value. This phenomenon can be explained with a basic addition of the Fe_3O_4 nanoparticles onto the surface of the Au layer. A change in the SPR angle is due to a change in the refractive index of the medium near the metal surface (Au surface). By the addition of the Fe_3O_4 nanoparticles so the refractive index of the medium will increase. Therefore, a larger signal of the SPR will be obtained with a small change in the refractive index of the medium (Antiochia, et al., 2016). These results are consistent with the research reported by (Oktivina, et al., 2017) which the SPR-angle shifted to 1° for a concentration of Fe_3O_4 of 11 mg/ml. The sensitivity of the biosensor was reported to be 0.093°±0.004° for every change of 1 mg/ml Fe_3O_4 nanoparticles' concentration. Moreover, Fe_3O_4 can be a signal amplifier for the SPR-based biosensor.

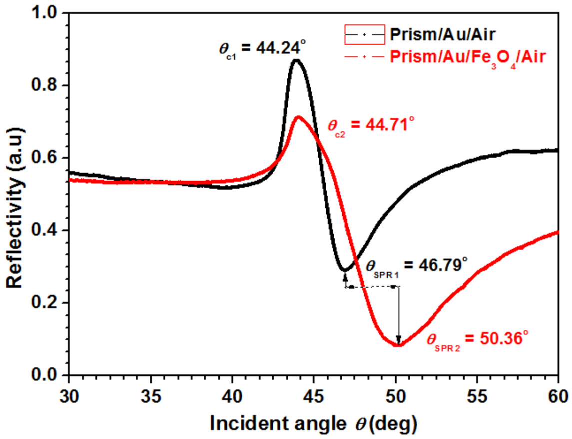

Figure 11. The ATR curves of SPR biosensor.

The significance of the Fe_3O_4 nanoparticles for this application was affected by the crystallinity, size distribution, morphology, and optical properties. Hence, a smaller crystallite size of the Fe_3O_4 nanoparticles will provide a larger specific surface area in which is very significant influence the process of signal amplification of the biosensor. The larger surface area of the Fe_3O_4 nanoparticles allows increasing the bonding surface between the analyte and the nanoparticles. The magnetic properties of the Fe_3O_4 principally influence the performance of biosensor. Unfortunately, in this research, we did not cover any explanation about the effect of the magnetic properties due to an absence of the external magnetic field, applied to the biosensor. Further, we didn't report yet about a specific analyte to be tested by using this biosensor. Therefore, further research is possible to be carried out for detecting any kind of analyte concerning the specific issue being discussed, for instance, urease, creatinine, glucose, or any compound in the human urine. This is concerning the issue of kidney failure.

CONCLUSIONS AND SUGGESTIONS

The Fe_3O_4 sample nanoparticles have been successfully synthesized by using the coprecipitation method at a temperature of 80°C with 5M NaOH and without the addition of heat treatment after synthesis. The nanoparticles have a crystallite size of 15.70 nm and a specific surface area of $73.00 \cdot 10^4$ cm^2/gram. Both electron diffraction and the vibration spectra have justified the formation of single-phase Fe_3O_4 nanoparticle with a soft-ferrimagnetic property at room temperature. The physicochemical properties of the Fe_3O_4 nanoparticle were strongly affected by the microstructural parameters. Moreover, the Fe_3O_4 nanoparticles have been proved to amplify the SPR signal of the biosensor.

Some drawbacks of this research have been discussed in detail. Firstly, further researches have to be conducted by significantly control the microstructure of the Fe_3O_4 by some efforts, i.e., controlling synthesis parameters, adding a surfactant, and further adding heat treatment for obtaining well-microstructural properties. A worse microstructural property will influence its significance for any applications, mainly in the field of SPR-based biosensor. Secondly, the biosensor with Fe_3O_4 nanoparticles can be carried out to detect the appearance of an analyte concerning the special issue being overcome. For instance, an issue of kidney failure gives a possibility to take such urease, creatinine, and glucose as samples of the analyte to be sensed.

AKNOWLEDGEMENTS

We would like thank to the Government of Indonesia due to fully financial support given by Kemenristek Dikti toward PDP Research Grant year 2018-2019 with a contract number of 118/SP2H/LT/DRPM/2019. We would also like thank to Universitas Halmahera throughout LPPMP for facilitating the administration. The last, we would like to give a great thanks to Nanomagnetic Materials and Surface Physics Research Group at the Laboratory of Material Physics and Instrumentation, Department of Physics Universitas Gadjah Mada for the facilities and the laboratory services.

REFERENCES

Abd, A. N., Latif, D. M. A. & Abdulridha, W. M., 2016. Synthesis and Some Physical Properties of Magnetite (Fe_3O_4) NPs. *Journal of Multidisciplinary Engineering Science Studies,* 2(3), pp. 341-345.

Antiochia, R., Bollella, P., Favero, G. & Mazzei, F., 2016. Nanotechnology-Based Surface Plasmon Resonance Affinity Biosensors for In Vitro Diagnostics. *International Journal of Analytical Chemistry,* pp. 1-16.

Bain, A. K. & Chand, P., 2017. Dielectric Properties of Materials. In: *Ferroelectrics: Principles and Applications.* s.l.:Wiley-VCH Verlag GmbH & Co. KGaA., pp. 1-18.

Batool, R. et al., 2019. A Review of the Construction of Nano-Hybrids for Electrochemical Biosensing of Glucose. *Biosensors,* 9(46), pp. 1-19.

Chaki, S. H. et al., 2015. Magnetite Fe_3O_4 Nanoparticles Synthesis by Wet Chemical Reduction and Their Characterization. *Advances in Natural Sciences: Nanoscience and Nanotechnology,* Volume 6, pp. 1-7.

Cui, L. et al., 2018. An Ultrasensitive Electrochemical Biosensor for Polynucleotide Kinase Assay based on Gold Nanoparticle-Mediated Lambda Exonuclease Cleavage-Induced Signal Amplification. *Biosensors and Bioelectronics,* Volume 99, pp. 1-7.

Dhas, C. R. et al., 2015. Visible Light Driven Photocatalytic Degradation of Rhodamine B and Direct Red using Cobalt Oxide Nanoparticles. *Ceramics International,* Volume 41, p. 9301–9313.

Ekariyani, N. Y. et al., 2016. *The use of Fe_3O_4 Magnetic Nanoparticles as the Active Layer to Detect Plant's DNA with Surface Plasmon Resonance (SPR) based Biosensor.* s.l., American Institute of Physics, p. 150016.

Ghandoor, H. E., Zidan, H. M., Khalil, M. K. H. & Ismail, M. I. M., 2012. Synthesis and Some Physical Properties of Magnetite(Fe_3O_4) Nanoparticles. *International Journal of Electrochemical Science,* Volume 7, pp. 5734 - 5745.

Hafez, M., Yahia, I. S. & Taha, S., 2014. Diffused Reflectance and Structure Analysis for the Nano-matrix ($ZnO_{(1-x)}SiO_{2(x)}$) System. *Spectrochimica Acta Part A: Molecular and Biomolecular Spectroscopy,* Volume 127, p. 521–529.

Heiba, Z. K., Mohamed, M. B. & Wahba, A. M., 2016. Effect of Mo Substitution on Structural and Magnetic Properties of Zinc Ferrite Nanoparticles. *Journal of Molecular Structure,* Volume 1108, pp. 347-351.

Huili, H. et al., 2014. Effect of Sintering Conditions on the Structural, Electrical, and Magnetic Properties of Nanosized $Co_{0.2}Ni_{0.3}Zn_{0.5}Fe_2O_4$. *Ceramics International,* Volume 24, pp. 1-14.

Indrayana, I. P. T., Tjuana, L. A., Tuny, M. T. & K., 2019. *Nanostructure and Optical Properties of Fe_3O_4: Effect of Calcination Temperature and Dwelling Time.* Makassar, IOP Publishing, pp. 1-8.

Jamil, N. A. B. et al., 2017. *Urea Biosensor utilizing Graphene-MoS_2 and Kretschmann-based SPR.* Malysia, IEEE, pp. 1973-1977.

Laksono, F. D., Supardianningsih, Arifin, M. & Abraha, K., 2018. *Development of Low Cost and Accurate Homemade Sensor System Based on Surface Plasmon Resonance (SPR).* Yogyakarta, IOP Publishing, pp. 1-7.

Malega, F., Indrayana, . I. P. T. & Suharyadi, E., 2018. Synthesis and Characterization of the Microstructure and Functional Group Bond of Fe_3O_4 Nanoparticle from Natural Iron Sand in Tobelo North Halmahera. *Jurnal Ilmiah Pendidikan Fisika Al-BiRuNi,* 7(2), pp. 13-22.

Mehrotra, P., 2016. Biosensors and Their Applications – A Review. *Journal of Oral Biology and Craniofacial Research,* Volume 6, pp. 153-159.

Mote, V. D., Dargad, J. S. & Dole, B. N., 2013. Effect of Mn Doping Concentration on Structural, Morphological and Optical Studies of ZnO Nano-particles. *Nanoscience and Nanoengineering,* 1(2), pp. 116-122.

Oktivina, M. et al., 2017. *Effect of Fe_3O_4 Magnetic Nanoparticle Concentration on the Signal of Surface Plasmon Resonance (SPR) Spectroscopy.* s.l., IOP Publishing Ltd., p. 012032.

Rahmawati , R. et al., 2018. Synthesis of Magnetite (Fe_3O_4) Nanoparticles from Iron Sands by Coprecipitation-Ultrasonic Irradiation Methods. *Journal of Materials and Environmental Sciences,* 9(1), pp. 155-160.

Ramadan, W., Kareem, M., Hannoyer, B. & Saha, S., 2011. Effect of pH on the Structural and Magnetic Properties of Magnetite Nanoparticles Synthesised by Co-precipitation. *Advanced Materials Research,* Volume 324, pp. 129-132.

Salazar, J. R. M., Camacho, S., Constantino, C. L. & Junior, O. N. O., 2018. New Trends in Plasmonic (Bio) Sensing. *Anaisda Academia Brasileira de Ciências,* 90(1), pp. 779-801.

Salviano, L. B. et al., 2018. Microstructural Assessment of Magnetite Nanoparticles (Fe_3O_4) Obtained by Chemical Precipitation Under Different Synthesis Conditions. *Materials Research,* 21(2), pp. 1-7.

Sati, A. et al., 2019. Direct Correlation Between the Band Gap and Dielectric Loss in Hf doped $BaTiO_3$. *Journal of Materials Science: Materials in Electronics,* pp. 1-7.

Singh, S., Mishra, S. K. & Gupta, B. D., 2013. Sensitivity Ehancement of a Surface Plasmon Resonance Based Fibre Optic Refractive Index Sensor Utilizing an Additional Layer of Oxides. *Sensors and Actuators A: Physical,* Volume 193, p. 136– 140.

Tajabadi , M. & Khosroshahi, M. E., 2012. Effect of Alkaline Media Concentration and Modification of Temperature on Magnetite Synthesis Method Using $FeSO_4/NH_4OH$. *International Journal of Chemical Engineering and Applications,* 3(3), pp. 206-210.

Tareq, R., Akter, N. & Md, A. S., 2019. Biochars and Biochar Composites: Low-Cost Adsorbents for Environmental Remidiation. In: *Biochar from Biomass and Waste.* s.l.:Elsevier Inc., pp. 169-209.

Wang, J. et al., 2010. Amino-Functionalized $Fe_3O_4@SiO_2$ Core–Shell Magnetic Nanomaterial as a Novel Adsorbent for Aqueous Heavy Metals Removal. *Journal of Colloid and Interface Science,* Volume 349, p. 293–299.

Widayanti, Abraha, K. & Utomo, A. B. S., 2018. Computational Study of Sensitivity Enhancement in Surface Plasmon Resonance (SPR) Biosensors by Using the Inclusion of the Core-Shell for Biomaterial Sample Detection. *Biosensors,* 8(75), pp. 1-14.